Research Square

Preprints are preliminary reports that have not undergone peer review.
They should not be considered conclusive, used to inform clinical practice,
or referenced by the media as validated information.

Spatio-temporal changes and hydrological forces of wetland landscape pattern in the Yellow River Delta during 1986-2022

Mengqi Qiu
Beijing Normal University
Yanxu Liu
yanxuliu@bnu.edu.cn
Beijing Normal University
Peng Chen
Beijing Normal University
Naijie He
Soochow University
Shuai Wang
Beijing Normal University
Bojie Fu
Beijing Normal University

Research Article

Keywords: Salt marsh vegetation, time series, vegetation classification, hydrologic drivers, landscape indices

Posted Date: September 9th, 2023

DOI: https://doi.org/10.21203/rs.3.rs-3328023/v1

License: This work is licensed under a Creative Commons Attribution 4.0 International License. Read Full License

Additional Declarations: No competing interests reported.

Version of Record: A version of this preprint was published at Landscape Ecology on February 19th, 2024. See the published version at https://doi.org/10.1007/s10980-024-01850-y.

Abstract

Context:

Estuarine wetlands provide valuable ecosystem services but have undergone continuous change under the pressures of climate change and anthropogenic disturbance. The Yellow River Delta (YRD) wetland, which is one of the most vigorous delta areas in the world, has undergone dramatic changes. However, the long-term and high-resolution typical salt marsh vegetation evolution processes and hydrological drivers remain unclear.

Objectives

(1) Generate annual mapping of salt marsh vegetation in the YRD wetland from 1986 to 2022. (2) Analyze the trends of wetland patch area and landscape pattern, and explain the hydrological drivers of landscape pattern evolution.

Methods

Combining Landsat 5–8 and Sentinel-2 images, vegetation phenology, remote sensing indices, and Random Forest supervised classification to map the typical salt marsh vegetation. We applied piecewise linear regression model to analyze YRD wetland changes, and stepwise multiple linear regression was used for assessing the impact of hydrological factors on landscape pattern.

Results

We identified three stages of landscape pattern evolution with 1997 and 2009 as turning points, including the rapid expansion stage, gradual decline stage, and bioinvasion stage. In the first phase, the wetland area was expanded by 70.45%, while the typical salt marsh vegetation, *Phragmites australis* area was reduced by 25%. In the second phase, the wetland was reduced by 21.33% and the *Phragmites australis* area was reduced by 15.96%. The third stage, *Spartina alterniflora* demonstrated an unstoppable trend of rapid expansion, with an area increase of 68 times relative to 2009, expanding at an average rate of 344 hm^2 per year.

Conclusions

Areas of wetland, tidal flat, and *Phragmites australis* are significantly influenced by cumulative sediment and cumulative runoff, which total explain 61.5%, 75.7% and 63.8% of their variations, respectively. Wetland and tidal flat areas increased with the cumulative sediment, while cumulative runoff had a weak negative effect. As for *Phragmites australis*, cumulative runoff had a positive effect, whereas cumulative sediment had a negative effect. Water resources regulation measures should be taken to prevent the degradation of wetland ecosystems, and intervention measures can be implemented during the seedling stage to control the invasion of *Spartina alterniflora*.

1 Introduction

Estuarine deltas present a global hotspot for ecological conservation and socio-economic development (Nienhuis et al. 2020; Reader et al. 2022). These deltas, characterized by fertile arable land, integrated transport nodes driving modern industry, and bountiful aquatic resources sustaining human populations, stand as the superior cradle of human civilization and cluster of metropolis (Loucks, 2019; Y. Chen & Kirwan, 2022; Törnqvist, 2023). Although they cover a mere 0.56% of the Earth's surface, estuarine deltas house 4.1% of the global population, with more than 339 million people living there (Edmonds et al., 2020). Wetlands in the estuarine delta have a unique coastal ecosystem, providing a wide range of ecological services, including

climatic regulation, carbon sequestration and biodiversity conservation (Xia et al. 2020; Reid, 2005). Unfortunately, estuarine wetlands are dynamic, sensitive and vulnerable systems (Ward et al. 2020), which are easily disturbed by environmental changes (e.g. flood, saltwater intrusion, sea level rise and biological invasion) (Barbier, 2014; Cox et al. 2022), coupled with anthropogenic pressures (e.g. agricultural expansion, urbanization and water conservancy project) (Murray et al. 2022; Lin & Yu, 2018). In such a complicated and volatile environment, estuarine wetlands are facing serious risks of area loss and ecological degradation (S. Li et al. 2022). It is estimated that 20–78% of coastal wetlands are expected to be lost by the end of the century, resulting in a profound erosion of biodiversity and an increased risk of flooding (Spencer et al. 2016; Rodríguez et al. 2017). Therefore, precise monitoring of the dynamic spatio-temporal patterns within wetland landscapes is critical for effective conservation, restoration and sustainable management of delta wetlands.

Recent studies on estuarine wetlands primarily focus on area gains and losses driven by human activities and natural processes (Osland et al. 2022; Nienhuis et al. 2020; Edmonds et al. 2023), Geomorphic changes especially under hydrology and hydrodynamics (Paszkowski et al. 2021), as well as ecosystem services assessment (Rosentreter et al. 2023). Murray et al. (2022) used Landsat images to assess the global tidal wetlands over the past two decades, and found that over 13,000 km^2 of tidal wetlands have recently been lost, but which has been offset by the creation of new wetlands mostly. Lin & Yu. (2018) interpreted coastal wetland distribution maps of three coastal city clusters in China, found that ecological degradation caused serious temporal loss of the remaining natural coastal wetlands in coincidence with the land conversion loss during the urbanizing period. However, the lack of detailed time series information hinders the accurate identification of regime shifts in estuarine wetland evolution, and increases the uncertainty of identified driving factors due to inconsecutive time series (X. Wang et al. 2021a). Considering the significant advantages of the Sentinel-2 dataset in terms of resolution (up to 10m), it enables the possibility of long-term and high spatiotemporal resolution wetland mapping (Chang et al. 2022; Zhou, 2022; Dong et al. 2016), and can deepen our comprehension of the multiple hydrological driving forces on the regime shifts of estuarine wetland evolution (Goldberg et al. 2020; Murray et al. 2019).

China's Yellow River is the most sediment-filled river on Earth (Song et al. 2020; Wang et al. 2007). Outstanding sediment brings excellent land-building function to the Yellow River Delta (YRD) wetland, which is considered to be one of the highest ecological conservation values among the river deltas in China (Cong et al. 2019). Although YRD wetland has been designated as a national nature reserve in 1992, listed in the Ramsar Convention on Wetlands in 2013, and approved for the construction of the Yellow River Delta National Park in 2021, the intensification of anthropogenic pressure and the growing impacts of environmental change are still continually affecting its tidal wetlands and their component intertidal ecosystems (X. Zhang et al. 2021; L. Li et al. 2023). Vegetation of estuary wetlands plays a key role in stabilizing the coast and accreting sediment to mitigate the negative impact of sea level rise (Pang et al. 2023). Salt marsh vegetation in the YRD wetland has evolved rapidly and coupled with the rapid invasion of *Spartina alterniflora* (SA*)* in recent years, the degeneration of native populations such as *Phragmites australis* (PA), which dominates wetland biodiversity and carbon sink capacity, has led to a sharp decline in the populations of rare waterfowl that live in habitats containing PA, and thus, the biodiversity of these wetlands is seriously threatened (C. Zhang et al. 2021). Current monitoring of YRD wetlands mainly focuses on artificial and natural wetlands (L. Li et al. 2023; Zhan et al. 2023), or single ecosystem types such as coastal vegetation, or woodland and grassland (A. Chen et al. 2016; L. Li et al. 2023). According to the difficulty to distinguish salt marsh vegetation from remote sensing images, not only monitoring of composite ecosystems is inadequate, but also the long-term and continuous interpretation is scarce (Cong et al. 2019; L. Li et al. 2023). Moreover, significant changes have taken place in the Yellow River's runoff (RU) and sediment discharge (SE) in the past 60 years (Song et al. 2020; S. Wang et al. 2016), which will have an important impact on the estuary wetland landscape pattern change, and regime shift may happen. Therefore, the understanding of the interactions between various hydrological factors and vegetation-type succession in wetland landscapes and ecosystems, as well as the impacts of these multiple driving factors on wetland evolution in the YRD, needs to be updated.

In order to explore the evolution trend of wetland landscape pattern in the YRD wetland and its hydrological driving factors, the objectives of this study are as follows. (1) to generate a complete time series mapping of salt marsh vegetation in the

YRD from 1986 to 2022 using Landsat 5/7/8 and Sentinel-2 satellite datasets, employing a Random Forest supervised classification method (the YRD wetland was classified into four types: water body, tidal flat, PA, and SA. Later, based on field surveys and visual interpretation, additional land cover types such as oilfield, pond, aquaculture, salt pan, and cultivated land were included. (2) analyzing the trends of wetland patch area and landscape pattern, and explaining the hydrological drivers of landscape pattern evolution in the YRD wetland by exploring the potential associations between wetland patches area, landscape indices and hydrological factors (such as RU, SE, cumulative runoff (RU+) and cumulative sediment (SE+)).

2 Methods

2.1 Study area

The YRD wetland is located at the mouth of the Yellow River in Dongying City, Shandong Province, facing the Bohai Sag to the east and the West Pacific to the west, backing to the Eurasian continent, between 37°61'— 37°89'N and 119°06'— 119°40'E, with an area of 883.26 km^2, and the average elevation is about 2—10m (Fig. 1a, b). Since the Yellow River formed, it has undergone 26 major channel shifts in history (Fig. 1a). Our study area is the modern estuary that stabilized after 1976, developed over nearly half a century, it has formed the world's terrestrial fastest-growing delta in terms of land area, representing a typical newly-formed estuarine wetlands worldwide.

Influenced by soil salinity gradients, the vegetation composition across the YRD wetland delineates a distinct zonal distribution, with SA, *Suaeda salsa*, and PA occupying sequential niches from the coast to the inland regions (Feng et al. 2018). PA, a dominant freshwater species, mainly thrives in wetland water bodies and along Yellow River banks (Fig. 1c2-c4). It serves as vital habitat for rare and endangered bird species and wetland animals, playing a critical role in biodiversity preservation and ecological integrity (C. Zhang et al. 2021). While, the SA is a typical halophytic plant, which primarily flourishes within intertidal zones along the coastal periphery and tidal flats (Wan et al. 2009) (Fig. 1c2-c4). It was once considered a "beach protector" due to its ability to stabilize shores, promote sediment deposition, resist typhoons, and reduce wave impact (Sun et al. 2023). However, propelled by its robust salt tolerance, flood tolerance, and reproductive capacity, it has rapidly spread along the Chinese coastal zone, posing a significant threat to biodiversity (Chang et al. 2022; Huang et al. 2022).

2.2 Datasets

2.2.1 Image data and processing

A total of 1728 surface reflectance images over the period 1986–2022 were selected from the Landsat-5 TM, Landsat-7 ETM+, Landsat-8 OLI (the scene of 121/34) and Sentinel-2 MSI (scenes of 50SPG and 50SQG) datasets with the spatial resolution of 30 m, which all available from the Google Earth Engine (GEE) cloud computing platform. For the Landsat series datasets, we adopted the Level 2, Collection 2, and Tier 1 version, which have been subject to systematic radiometric and geometric correction by the United States Geological Survey (Google, 2023a). The Sentinel-2 MSI Level-2A imagery, with a spatial resolution of 10—60 m, not only reduces the impact of atmospheric interference on the spectral measurements, but also includes cloud and atmospheric masks, exhibiting excellent performance in quantitative analysis of surface landscape (Google, 2023b). The number of Landsat images varies by season and year (Fig. 2a1, a2), averaging 17 images annually. In contrast, the annual average for Sentinel-2 imagery is significantly higher at 294 images. Finally, we used the median composite of all images for each phenological period as the image data for supervised classification.

2.2.2 Hydrological data

Hydrological data were sourced from the hydrological monitoring station located at Lijin, which is situated in the lowest downstream region of the Yellow River Basin. Specifically, we obtained the annual discharge and sediment load data from

1986 to 2021 for the Lijin station, which were acquired from the Yellow River Conservancy Commission of the Ministry of Water Resources.

2.3 Classification and Assessment

2.3.1 Phenology identification

PA and SA share remarkable morphological and color similarities, which create significant challenges for accurate cross-temporal supervised classification (Chang et al. 2022). However, there exist discernible differences in the phenology of these saltmarshes, providing an opportunity for differentiation. Both the Normalized Difference Vegetation Index (NDVI) and Enhanced Vegetation Index (EVI) serve as widely used indices for precise vegetation monitoring (Shammi & Meng, 2021; Bolton & Friedl, 2013). Consequently, we constructed monthly NDVI and EVI time series curves spanning a decade (2011–2021) to elucidate the phenological characteristics of these two saltmarshes.

Prior evidences indicate that PA's growth spans April to October, peaking between late July and early August, whereas SA's growth lags behind PA in the YRD wetland by about a month (Chang et al. 2022; C. Zhang et al. 2021). Therefore, we synthesized remote sensing imagery for three timeframes in 2021: April to June, June to October, and October to November, and displayed in a false-color composite of near-infrared, infrared, and green bands (Fig. 1c2-c4). These composites revealed distinct color variations for PA and SA throughout these periods: (1) From April to June, PA displayed a bright red shade, while SA exhibited a brownish hue. (2) From June to October, SA's color gradually shifted to a deeper red tone, surpassing the intensity of red in PA and becoming a dark red color. (3) From October to November, PA's color faded, transitioning to a reddish-brown shade, whereas SA appeared as a bright red color. Subsequently, we incorporated PA and SA samples into the GEE platform for the 2011–2021 period, with varying sample numbers across different years (Fig. 2c). Ultimately, monthly NDVI and EVI time series curves were generated for PA and SA (Fig. 2b1-b2).

The phenological cycle of PA includes four stages: seedling, growth, maturity, and senescence (Fig. 2b1). PA experiences vigorous growth from April to June, evident in rising NDVI and EVI curves. From June to August, PA's vegetation follows a bimodal pattern, reaching its annual peak, the maturity stage. Post-August, there's a rapid decline, marking the senescence period. In contrast, SA's growth phase lasts longer (Fig. 2b2), spanning five months, beginning gradually in April, accelerating until July, and peaking in September. However, after reaching its peak, SA swiftly enters the senescence phase.

2.3.2 Feature indices

Wetlands in YRD were primarily classified into three main types: salt marsh vegetation, tidal flat, and water body, with a further subdivision of PA and SA within the salt marsh vegetation. To facilitate precise monitoring, we incorporated five commonly used remote sensing indices: NDVI, EVI, Normalized Difference Water Index (MDWI), Modified Normalized Difference Water Index (mNDWI), and Land Surface Water Index (LSWI) (Eq. 1–5). Specifically, NDVI and EVI were employed for vegetation detection, MDWI and mNDWI for surface water detection, and LSWI as an auxiliary index for identifying green vegetation (Y. Li et al. 2022; Zeng et al. 2022). In addition, we refer to monitoring algorithms developed in recent research studies (X. Wang et al. 2021b) specifically for extracting coastal vegetation (Cveg) and coastal water bodies (Cwat) (Eqs. 6 and 7).

$NDVI = \frac{\rho_{nir} - \rho_{red}}{\rho_{nir} + \rho_{red}}$	(1)
$\mathrm{EVI} = 2.5 \times \frac{\rho_{nir} - \rho_{red}}{\rho_{nir} + 6 \times \rho_{red} - 7.5 \times \rho_{blue} + 1}$	(2)
$NDWI = \frac{\rho_{\mathrm{green}} - \rho_{\mathrm{nir}}}{\rho_{\mathrm{green}} + \rho_{\mathrm{nir}}}$	(3)
$\mathrm{mNDWI} = \frac{\rho_{\mathrm{green}} - \rho_{swir1}}{\rho_{\mathrm{green}} + \rho_{swir1}}$	(4)
$LSWI = \frac{\rho_{nir} - \rho_{swir1}}{\rho_{nir} + \rho_{swir1}}$	(5)
$\mathrm{Cveg} = (EVI \geq 0.1)\, and\, (NDVI \geq 0.2)\, and\, (LSWI > 0)$	(6)
$\mathrm{Cwat} = (mNDWI > EVI or NDWI > EVI) and (EVI < 0.1)$	(7)

Where $\rho_{blue}, \rho_{\mathrm{green}}, \rho_{red}, \rho_{nir}, and \rho_{swir1}$ are the surface reflectance values of blue, green, red, near-infrared, and shortwave infrared1 bands in Landsat 5/7/8 and Sentinel-2 images.

2.3.3 Supervisory classification and accuracy assessment

Random Forests (RF) model is a widely employed machine learning method for supervisory classification in remote sensing applications (Belgiu & Drăguţ, 2016; Stumpf & Kerle, 2011;Watts et al. 2009; P. Chen et al. 2022), which combines the strength of decision trees with random subsampling and feature selection. However, the model has exhibited relatively low sensitivity to overfitting, while displaying higher sensitivity to the selection of sampling points (Belgiu & Drăguţ, 2016; Rodriguez-Galiano et al. 2012). Given the significant inter-annual variability in the YRD wetland, the identification of reliable sample points that span across different years is a challenge. Therefore, we selected new samples nearly every year, with a total of 4391 samples throughout the time series (Fig. 2c).

The whole supervisory classification process can be divided into the following steps: (1) adding sample points through the optimal phase remote sensing images, (2) following the image processing approach used for phenology extraction, we synthesized remote sensing images for each of the three periods and inputting the feature indices bands for supervised classification, (3) obtained the preliminary annual supervised classification maps as a result. Due to the significant striping artifacts in the ETM + imagery in 2011, the mapping results were subject to considerable errors, therefore, (4) for the year 2011, we only selected the imagery from the less-affected period of 6 to 10 months for training, (5) manually corrected erroneous patches based on field surveys and visual interpretation, including oilfield, cultivated land, aquaculture, salt pan, and delineated ponds from the water body within the terrestrial interior of the wetland (Fig. 1c1), (6) for estimating how well the resulting RF model performs, 70% of the samples were used to train the trees with the remaining 30% were used in an internal cross-validation technique, then generated a confusion matrix, and calculated of the kappa coefficient and accuracy.

2.4 Statistical analysis

2.4.1 Landscape indices

Landscape indices are quantitative measures used to assess and describe the spatial arrangement and composition of landscapes (Tischendorf, 2001). These indices provide valuable insights into the structure, connectivity, fragmentation, and heterogeneity of landscapes, gaining a deeper understanding of landscape dynamics and ecological processes (H. Li & Wu, 2004). Here, we selected nine landscape pattern indices (Table 1) to quantitatively describe the landscape pattern of the YRD

wetland in five dimensions: area, landscape fragmentation, shape, diversity and aggregation. Then, we calculated the landscape pattern index of the YRD wetland from 1986 to 2022 using Fragstats 4.2.1 software.

Table 1
Landscape indices, dimensions and meanings.

Dimensions	Landscape indices	Meanings
area	largest patch index (LPI)	percentage of the largest patch of a landscape
fragmentation	interspersion and juxtaposition Index (IJI)	arrangement and interspersion of landscape
	splitting index (SPLIT)	splitting or fragmentation of patches
	patch density (PD)	number of patches per unit area in a landscape
shape	landscape shape index (LSI)	the complexity of patch shapes in a landscape
	perimeter-area fractal dimension (PAFRAC)	irregularity and complexity of patch boundaries
diversity	Shannon's evenness index (SHEI)	evenness or uniformity of patches
aggregation	aggregation Index (AI)	spatial clustering or aggregation of landscape
	contagion (CONTAG)	reflect the connectivity of the landscape

2.4.2 Regression analysis

We calculated the inter-annual variation and trends in YRD wetland for the period 1986–2022 through piecewise linear regression models with a test at the 5% significance level.

To assess the impact of long-term hydrological processes on wetland areas, we employed a stepwise multiple linear regression model. This model necessitates comprehensive diagnostic evaluations, encompassing three key aspects: collinearity, significance, and the Durbin-Watson (DW) test. Collinearity indicates a high correlation among independent variables, with a Variance Inflation Factor (VIF) exceeding 10 signifying strong collinearity. Significance assessment relies on the P-value for regression coefficients, with P-values below 0.05 allowing rejection of the null hypothesis. Lastly, the DW test detects autocorrelation in regression model residuals, with critical values determined based on sample size (n) and the number of independent variables (k) using a table lookup method.

We established the potential relationships between SE, RU, SE+, RU + and landscape indices to explore the factors driving landscape pattern evolution in the YRD wetland. Firstly, we examined the correlation between hydrological data and landscape indices, including the Pearson correlation coefficient and Spearman correlation coefficient. Secondly, based on the correlation coefficients, we established three distinct conditions for further analysis. Condition 1: using the Pearson correlation coefficient, we selected variables with $P < 0.001$ and conducted simple linear regression between the qualifying landscape pattern indices and the hydrological variables that exhibited a significant influence. Condition 2: for landscape indices that did not meet Condition 1, we used the Spearman correlation coefficient and selected two hydrological variables that simultaneously satisfied $P < 0.001$ or $P < 0.01$, then performed either multivariate nonlinear fitting or segmented linear fitting. Condition 3: if none of the conditions were met, we exclusively plotted scatter plots of the hydrological variables that demonstrated higher correlation coefficients. Through these systematic steps, our goal was to investigate the relationships between each landscape index and its statistically significant hydrological processes.

3 Results

3.1 Spatial changes of YRD wetland during 1986–2022

A total of 37 spatial distribution maps depicting the typical salt marsh vegetation in the YRD wetland for the period 1986–2022 were generated. The overall classification accuracy exceeded 96%, with a minimum Kappa coefficient value of 0.94, indicating that our classification results are reliable and highly accurate (Fig. 2c). Over the course of these 37 years, we present eight maps that are representative (Fig. 3). It is evident that in the past four decades, the YRD wetland has undergone substantial changes in terms of morphology, riverine pathways, and typical salt marsh vegetation.

In the early stages of the formation of the YRD, 1986, the wetland exhibited a relatively regular and open elliptical shape, with the typical salt marsh vegetation, PA, primarily distributed along the inland tidal flats on both sides of the Yellow River. Subsequently, as river erosion intensified, by 1990, the shape of the wetland became increasingly pointed, resembling a bird's beak.

Later, in 1996, a watershed year for the YRD wetland, the long-established southeastward outlet channel was abandoned, giving way to a new northeastward channel. Initially, the new channel had a smaller mouth, but after nearly 10 years of development, by 2006, the northeastward channel gradually expanded, and formed one of the two major branches of the YRD wetland, alongside the southeastward channel, making it a remarkable phenomenon among estuarine wetlands worldwide. Furthermore, in 2006, extensive seasonal water ponds started to emerge in the southern part of the YRD wetland.

In 2009, the fragmented patches of SA began to be observed, particularly close to the coastal tidal flat. Additionally, human activities such as aquaculture ponds, cultivated land, and salt fields gradually became evident during the same year. By 2012, the northeastern branch of the new flow path had further extended towards the ocean. And near the coastal areas, apparent patches of SA were observed, indicating its successful colonization. Simultaneously, larger seasonal water ponds appeared in the northern part of the YRD wetland.

Over the subsequent decade, the SA flourished and expanded its dominion, progressively extending its territory from the coastal tidal flats towards the inland areas. Meanwhile, the SA, itself has become another dominant species, soaring to prominence in this ecosystem. Furthermore, in 2022, it started to challenge the established dominant species in the region, the PA, which traditionally thrived along the Yellow River, that gradually encroached upon its stronghold. Moreover, the morphological transformation of the YRD wetland during this period witnessed the continuous strengthening of the northeastern flow path, while the southeastern flow path gradually declined.

3.2 Patch area changes of YRD wetland during 1986–2022

Through visualizing the temporal changes of patches area in the YRD wetland over the past 37 years, we identified three stages of landscape pattern evolution: rapid expansion stage, gradual decline stage, and bioinvasion stage (Fig. 4a). From 1986 to 1997 was the first stage of wetland expansion, during the 12 years, both wetland area and tidal flat area showed a rapid increase trend (R^2 = 0.91 for wetland area and tidal flat area), with a 70.45% increase in the wetland area, reaching the peak of the entire time series in 1997 at 387.62 km^2, which laid the foundation for the wetland pattern. While during this period, the dominant salt marsh vegetation, PA, was reduced by 25%. The second stage is the wetland decline stage, from 1997 to 2009, the wetland and tidal flat areas showed a slow decline trend (R^2 = 0.33, Pearson's r = -0.57 for wetland; R^2 = 0.58, Pearson's r = 0.76 for tidal flat area), with the area of wetland reduced by 21.33%, PA reduced by 15.96%. The third stage is the bioinvasion stage, SA demonstrated an unstoppable trend of rapid increase (R^2 = 0.93), with an area increase of 68 times relative to 2009, expanding at an average rate of 3.44 km^2 per year, approaching the area of PA by 2021 and becoming another dominant species in the YRD wetland. In the same term, the PA area increased by 17.62%, however, extensive tidal flat was being encroached upon by SA, resulting in its area being reduced by 23.02%.

Making a general observation of the transition matrix of patches area across the three stages (Fig. 4b), it can draw four findings: (1) the YRD wetland had undergone three different strengths of patch changes; (2) in the first stage, although there were significant variations in patch flows, the types of changes were relatively homogeneous; (3) in the second stage, there was a noticeable increase in human activities, leading to an increase in the transfer flows and the density of the flow

network; (4) in the third stage, although the single flow of patch transfers decreased, the transfer network became more complex.

In the first stage, the area of tidal flats doubled in size, with 161.77 km^2 contributed by wetland and 51.57 km^2 contributed by PA, indicating a certain degree of degradation in the PA ecosystem. In the second stage, an area of 35.19 km^2 of tidal flats transformed into wetlands, signifying increased seawater intrusion. Additionally, a small portion of the tidal flat was converted into a pond, salt pan, and cultivated land, indicating the manifestation of human activities. In the third stage, an area of 24.79 km^2 of tidal flat and 19.27 km^2 of water body were encroached upon by SA, while 38.38 km^2 of tidal flat was occupied by water body. Furthermore, an area of 19.55 km^2 of the water body transformed into a tidal flat, accounting for the tidal flat had experienced both erosion and deposition counterbalance in that time.

Compared to wetland patch area, the landscape indices can comprehensively reflect information about landscape composition and spatial configuration, representing a highly condensed characterization of landscape pattern features. The temporal variations of landscape indices from 1986 to 2022 displayed a dual-stage or tri-stage pattern, with notable differences observed in the timing and trends of various indices (Fig. 4c). LSI, SPLIT, LJI, and PD, these four landscape indices, which represent landscape shape complexity, fragmentation, interspersion and juxtaposition, and patch density, respectively, exhibiting two distinct stages with the year 2001 serving as the turning point. From 1986 to 2001, these indices displayed a decreasing trend ($0.33 \leq R^2 \leq 0.57$). However, after 2001, they exhibited a significant upward trend ($0.37 \leq R^2 \leq 0.92$). It is indicated that before 2001, the wetland tended to exhibit regularity and uniformity, while afterwards, it became increasingly fragmented with more complex shapes. AI reflects the connectivity between each patch type, in contrast, which exhibits a trend of initial increase followed by a decrease, with the year 2001 as a turning point.

LPI, representing the proportion of the largest patch in the wetland, showed a decreasing trend in 1997 ($R^2 = 0.78$) and remained relatively high thereafter. In the YRD wetland, the largest patch was the water body, which was replaced by the tidal flat during the wetland expansion stage. Subsequently, as the wetland gradually receded, the water body area increased, resulting in a consistent trend between LPI and the water body. SHEI exhibited a significant increasing trend before 1988 ($R^2 = 0.79$). A higher value of the index indicates a closer proportion of different patch types in the landscape and a higher level of evenness. This suggests that the evenness of the landscape continuously improved until 1998, after which it remained at a relatively low level. PAFRAC, reflecting the complexity of patch boundaries, gradually decreased before 1995 but experienced a sudden increase after 2006, maintaining a high level thereafter. Unlike AI, CONTAG reflects the overall connectivity of the landscape. Before 1998, the wetland exhibited poor connectivity with a declining trend ($R^2 = 0.67$). Subsequently, connectivity remained relatively high but also showed a decreasing trend.

3.3 Hydrological forces of wetland patch area

Stepwise linear regression results (Table 2) indicate that the dependent variables of wetland, tidal flat, and PA passed the model diagnostics ($P_i<0.001$, $1.35 < DW < 1.59$, at the significance level of 0.05, $n = 36$ and $k = 3$; $VIF_{3-4} < 10$). SA is likely limited by sample size, with high VIF and overfitting indicated by adjusted R^2, concluding that the model fails. Based on the model, the area of wetland, tidal flat, and PA in the YRD wetland are significantly influenced by SE + and RU+, explaining 61.5%, 75.7% and 63.8% of their variations respectively, while RU and SE are excluded from the model. Specifically, the wetland area and tidal flat area are positively correlated with the SE+ ($\beta_{31} = 2.61$, $\beta_{32} = 4.62$), while the RU + shows a weak negative effect ($\beta_{41} = -0.023$, $\beta_{42} = -0.063$). However, for PA, as a hydrophilic vegetation, the situation is the opposite as the RU + has a positive effect on its area ($\beta_{43} = 0.008$).

Table 2
Stepwise multiple linear regression results of YRD wetland patch area with hydrological variables. RU, SE+, RU + respectively represent runoff, cumulative runoff, and cumulative sediment transport. * means P ≤ 0.05, ** means p ≤ 0.01, and *** means P ≤ 0.001 (the same as below).

Patch area ($X_{i,\ i=1,2,3,4}$)	Adjusted R_i^2	DW_i	F_i	Constant	RU		SE+		RU+	
				β_{0i}	β_{1i}	VIF_1	β_{3i}	VIF_3	β_{4i}	VIF_4
Wetland	0.615	1.463	28.944	223.984***			2.611***	7.367	-0.023***	7.367
Tidal flat	0.757	1.516	55.488	141.277***			4.620***	7.367	-0.063***	7.367
PA	0.638	1.374	31.788	87.259***			-0.868***	7.367	0.008***	7.367
SA	0.989	2.262	282.100	235.371**	− .025*	3.898	-6.738***	141.503	0.066***	119.275

3.4 Hydrological forces of landscape pattern

The correlation between RU + and SE + with the landscape indices demonstrated a higher overall significance compared to RU and SE (Fig. 5a1-5a2). Specifically, significant simple linear correlations (P < 0.001) were found between RU and AI, IJI, LSI, and PD, with Pearson correlation coefficients of -0.58, 0.61, 0.57, and 0.65, respectively (Fig. 5a1). Furthermore, RU + demonstrated significant (P < 0.001) linear correlations with AI, SPLIT, IJI, LSI, and PD, with Pearson correlation coefficients of -0.61, -0.53, 0.68, 0.63, and 0.68, respectively. Additionally, significant monotonic correlations (P < 0.001) were observed between RU + and SHEI, CONTAG, with Spearman correlation coefficients of -0.57 and 0.55, respectively (Fig. 5a2).

In contrast, the correlation between SE and the landscape pattern of YRD wetland was overall not substantial. Among the landscape indices, SHEI and CONTAG exhibited highly significant (P < 0.001) correlations with respective Pearson correlation coefficients of 0.47 and − 0.50. SE + displayed significant (P < 0.001) linear correlations with SPLIT, CONTAG, and LPI, with Pearson correlation coefficients of 0.58, 0.53, and − 0.57, respectively (Fig. 5a1). Furthermore, SE + exhibited highly significant (P < 0.001) monotonic correlations with AI, SHEI, IJI, LSI, and PD, as indicated by respective Spearman correlation coefficients of -0.58, -0.57, 0.56, 0.60, and 0.62 (Fig. 5a2).

The indices that satisfied Condition 1 included PD, LSI, CONTAG, IJI, SPLIT, and AI. LPI and SHEI satisfied Condition 2, while the index that satisfied Condition 3 was PAFRAC.

The patch density (PD) in the YRD wetland increases with an increase in RU and RU+ (Fig. 5b1). PD is more sensitive to RU, but the impact of RU + on its variation is slightly greater (R^2 = 0.46). The two fitted curves of the landscape pattern index (LPI) are shown (Fig. 5b2). As RU + and SE + increase, the area of WA representing the largest proportion of landscape patches decreases, indicating an increase in the total wetland area. In other words, RU + and SE + promote the development of the YRD wetland, with both variables explaining 46% of the variation in LPI. The shape complexity, represented by the landscape shape index (LSI), significantly increases with the influence of RU and RU+ (Fig. 5b3). Similar to PD, LSI is more sensitive to RU, but the regression equation fitted with RU + performs better (R^2 = 0.39).

Among all the landscape indices, PAFRAC is the only index that is not sensitive to any of the hydrological features. This is shown in the scatter plot (Fig. 5b4), where most of the points are concentrated in the upper left quadrant, indicating a positive correlation with SE and RU, but without statistical significance. CONTAG, which reflects landscape connectivity, decreases with an increase in SE (R^2 = 0.30) (Fig. 5b5). However, it increases with an increase in SE+ (R^2 = 0.28), and it is more sensitive to SE. Similar to PD and LSI, RU and RU + have a significant promoting effect on IJI (Fig. 5b6), with explanatory values of 37% and 47%, respectively. This indicates that increased runoff intensifies the fragmentation of wetland patches.

SPLIT is significantly influenced by both RU + and SE+ (Fig. 5b7), and it increases with an increase in both variables. SHEI is a special landscape index that reflects landscape uniformity. The results indicate that when RU + at the Lijin station is within 2040.63×10^8 m^3 and SE + is within 53.94×10^8 t, SHEI increases significantly with RU + and SE+ (Fig. 5b8), with explanatory values of 82% and 79%, respectively. However, beyond these values, the scatter plot becomes disordered and remains at a lower level. In contrast to landscape fragmentation, AI, which reflects landscape spatial aggregation, decreases with an increase in RU ($R^2 = 0.34$) and RU+ ($R^2 = 0.37$) (Fig. 5b9).

4 Discussions

4.1 Spatial changes

The shape of a river delta is influenced by rivers, tides, and waves (Nienhuis et al. 2020). Accordingly, during the initial period, the morphology of the YRD was predominantly controlled by the river. However, in later stages, although the river discharge continued to play a dominant role, the influence of waves became more important. It is generally recognized that the morphology of YRD is primarily river-dominated, given its reputation for significant sediment loads, while a sharp decrease in sediment transport in the Yellow River (S. Wang et al. 2016). Before the Yellow River's course change in 1996, the morphology of the YRD exhibited a single lobe extending continuously towards the ocean. After the course change, the newly formed northeast channel experienced ongoing sediment deposition, while the southeastern abandoned channel mouth weakened under marine erosion. As for the diversion of the Yellow River estuary in 1996, this significant alteration that shapes the geomorphological structure of the estuary is driven by the imperative requirements of estuary management and development, involving artificial diversion (Yu et al. 2021). Therefore, throughout the entire time series, the morphological changes in the YRD are predominantly governed by the influential force of the river, with human activities playing a pivotal role as agents of transformative changes after 1996.

4.2 Patch area changes

From 1986 to 2022, the wetland area underwent rapid expansion, followed by a gradual decline, and then a slow increase (Fig. 6a). This trend is mainly influenced by SE + and RU+, with SE + playing a more significant role, positively affecting wetland area (Yu et al. 2021), while RU + has a weak negative impact (Fig. 6b).

The tidal flat area exhibited a pattern of initial increase followed by continuous decrease (Fig. 6a). In the first stage, the tidal flat area increased with rising SE+. In the second stage, 35.19 km^2 of tidal flats transitioned to seawater, while a small portion converted to ponds, salt fields, and cultivated land, indicating a consistent decline due to seawater intrusion and human activities. In the third stage, 24.79 km^2 of tidal flats were invaded by SA, and 18.83 km^2 were eroded by seawater. Consequently, invasive SA and seawater erosion were the primary causes of tidal flat reduction in the third stage.

The PA area continuously decreased in the first and second stages, but showed a slight rebound in the third stage (Fig. 6a). This was mainly influenced by RU + and SE+, where RU + played a positive role (Y. Zhang et al. 2022) and SE + had a negative effect (Fig. 6b). Furthermore, the rebound in the third stage might also be attributed to recent ecological conservation policies. For instance, since 2008, the Yellow River Commission has been conducting regular ecological replenishment to the YRD, promoting the recovery of the PA ecosystem.

For SA, in 2009, small patches were first observed in the YRD wetland. Around 2010, it rapidly expanded unstoppably, and its invasion mechanism is difficult to explain solely through mathematical models. However, research had shown that the density, height and basal diameter of SA increased with tidal inundation (Ma et al. 2019). Once the harm it caused was recognized, control measures such as "enclosure and flooding" and "cutting and ploughing" were implemented. By 2022, there was a slight decline of in SA area.

4.3 Landscape pattern changes

The YRD wetland landscape fragmentation, shape complexity and aggregation are primarily influenced by RU and RU+ (Fig. 6b). It implies that under the erosive forces of flowing water, estuarine wetland landscapes tend to exhibit fragmentation and increasing complexity in shape, resulting in a decrease in landscape aggregation, particularly during flood events (Liu et al. 2022).

The YRD wetland landscape connectivity is mainly influenced by SE and SE+, which have a positive impact. SE, which plays a significant role in shaping the connectivity of the YRD wetland (Fig. 6b). As sediment erodes and is transported by flowing water, it can contribute to the formation of channels, channel networks, and water pathways, enhancing the connectivity between different wetland areas. This promotes the exchange of water, nutrients, and biota within the wetland ecosystem, supporting the overall ecological health and functioning of the YRD wetland.

The hydrological driving effect on YRD patch evenness needs to be controlled within a certain range: when the Lijin Station's cumulative runoff (RU+) is almost lower than 2040×10^8 m^3 and cumulative sediment discharge (SE+) is almost lower than 54×10^8 t, the Shannon's Evenness Index (SHEI) significantly increases with the increase of RU + and SE+; which highlights the importance of regulating hydrological factors to achieve optimal patch evenness in the YRD wetland.

In addition, the landscape fragmentation, shape complexity, and aggregation are important turning points around 2001, which are likely related to the formal operation of the large-scale hydraulic project—Xiaolangdi Reservoir. As a major water diversion and sediment control project in the lower reaches of the Yellow River, the Xiaolangdi Reservoir regulates the runoff and sediment discharge downstream (X. Xia et al. 2016), and therefore is likely to be an important factor influencing the landscape pattern.

4.4 Sources of uncertainty

We generated high spatial and temporal resolution maps of typical salt marsh vegetation in the YRD wetland from 1986 to 2022, and analyzed its landscape pattern changes and hydrological driving factors, providing a quantitative basis for the scientific management of wetlands. However, due to the rapid changes in the landscape pattern of the YRD wetland, it is almost necessary to replace the sample points in GEE every year to achieve long-term supervised classification, and this visual-based sampling process may introduce potential and unavoidable errors. Moreover, the landscape pattern of the YRD wetland may also be influenced by other anthropogenic factors on landscape such as salt fields, cultivated land, and aquaculture ponds, which may also contribute to the recent increase in landscape fragmentation and shape complexity (G. Li et al. 2021).

5 Conclusions

By combining high-resolution remote sensing images, we generated a 30-meter resolution, annual time-scale dataset of typical salt marsh vegetation in the YRD from 1986 to 2022, and discussed the hydrological driving factors of wetland landscape evolution. We identified that the YRD has experienced three stages of landscape pattern changes with 1997 and 2009 as turning points, including the rapid expansion stage, gradual decline stage, and bioinvasion stage. Furthermore, in the most recent two decades, human footprints have encroached upon this natural wetland area intensively, and seawater intrusion is also taking place at the same time, threatening the tidal flat area. Moreover, with the increase of runoff and cumulative runoff, estuarine wetland landscapes tend to exhibit fragmentation and increasing shape complexity, resulting in a decrease in landscape aggregation. While sediment and cumulative sediment have a positive impact on wetland landscape connectivity. Measures should be taken to prevent the degradation of tidal flat and *Phragmites australis* areas, such as regulating sediment and runoff from upstream regions and implementing ecological replenishment. To control the extensive proliferation of *Spartina alterniflora*, intervention measures can be implemented during the seedling stage. The findings extended the theoretical basis of landscape regime shift for the conservation, management, and sustainable development of

the YRD wetland. Further exploring the factors of natural factors (such as climate change, sea-level rise, and seawater intrusion) and human factors (such as water conservancy projects, dam construction, expansion of cultivated land, and aquaculture) on the changes in salt marsh vegetation of estuarine wetland is recommended in future research.

Declarations

Author contributions

Mengqi Qiu: Methodology, Software, Validation, Writing - Original Draft, Writing - Review & Editing, Visualization.

Yanxu Liu: Resources, Writing - Review & Editing, Supervision, Funding acquisition.

Peng Chen: Software, Writing - Review & Editing.

Naijie He: Formal analysis.

Shuai Wang: Writing - Review & Editing.

Bojie Fu: Supervision.

Acknowledgements

This research was supported by the National Natural Science Foundation of China (No. 42041007) and the Fundamental Research Funds for the Central Universities of China.

Ethics approval and consent to participate are Not applicable.

Consent for publication is Not applicable.

Competing interests The authors declare that they have no known competing financial interests or personal relationships that could have appeared to influence the work reported in this paper.

Data availability statement

The datasets generated during and/or analysed during the current study are available from the corresponding author upon reasonable request.

References

1. Barbier, E. B. (2014). A global strategy for protecting vulnerable coastal populations. *Science*, *345*(6202), 1250–1251. https://doi.org/10.1126/science.1254629
2. Belgiu, M., & Drăguţ, L. (2016). Random forest in remote sensing: A review of applications and future directions. *ISPRS Journal of Photogrammetry and Remote Sensing*, *114*, 24–31. https://doi.org/10.1016/j.isprsjprs.2016.01.011
3. Bolton, D. K., & Friedl, M. A. (2013). Forecasting crop yield using remotely sensed vegetation indices and crop phenology metrics. *Agricultural and Forest Meteorology*, *173*, 74–84. https://doi.org/10.1016/j.agrformet.2013.01.007
4. Chang, D., Wang, Z., Ning, X., Li, Z., Zhang, L., & Liu, X. (2022). Vegetation changes in Yellow River Delta wetlands from 2018 to 2020 using PIE-Engine and short time series Sentinel-2 images. *Frontiers in Marine Science*, *9*, 977050. https://doi.org/10.3389/fmars.2022.977050
5. Chen, A., Sui, X., Wang, D., Liao, W., Ge, H., & Tao, J. (2016). Landscape and avifauna changes as an indicator of Yellow River Delta Wetland restoration. *Ecological Engineering*, *86*, 162–173. https://doi.org/10.1016/j.ecoleng.2015.11.017

6. Chen, P., Wang, S., Liu, Y., Wang, Y., Li, Z., Wang, Y., Zhang, H., & Zhang, Y. (2022). Spatio-temporal patterns of oasis dynamics in China's drylands between 1987 and 2017. *Environmental Research Letters*, *17*(6), 064044. https://doi.org/10.1088/1748-9326/ac740b
7. Chen, Y., & Kirwan, M. L. (2022). Climate-driven decoupling of wetland and upland biomass trends on the mid-Atlantic coast. *Nature Geoscience*, *15*(11), Article 11. https://doi.org/10.1038/s41561-022-01041-x
8. Cong, P., Chen, K., Qu, L., & Han, J. (2019). Dynamic Changes in the Wetland Landscape Pattern of the Yellow River Delta from 1976 to 2016 Based on Satellite Data. *Chinese Geographical Science*, *29*(3), 372–381. https://doi.org/10.1007/s11769-019-1039-x
9. Cox, J. R., Paauw, M., Nienhuis, J. H., Dunn, F. E., van der Deijl, E., Esposito, C., Goichot, M., Leuven, J. R. F. W., van Maren, D. S., Middelkoop, H., Naffaa, S., Rahman, M., Schwarz, C., Sieben, E., Triyanti, A., & Yuill, B. (2022). A global synthesis of the effectiveness of sedimentation-enhancing strategies for river deltas and estuaries. *Global and Planetary Change*, *214*, 103796. https://doi.org/10.1016/j.gloplacha.2022.103796
10. Dong, J., Xiao, X., Menarguez, M. A., Zhang, G., Qin, Y., Thau, D., Biradar, C., & Moore, B. (2016). Mapping paddy rice planting area in northeastern Asia with Landsat 8 images, phenology-based algorithm and Google Earth Engine. *Remote Sensing of Environment*, *185*, 142–154. https://doi.org/10.1016/j.rse.2016.02.016
11. Edmonds, D. A., Caldwell, R. L., Brondizio, E. S., & Siani, S. M. O. (2020). Coastal flooding will disproportionately impact people on river deltas. *Nature Communications*, *11*, 4741. https://doi.org/10.1038/s41467-020-18531-4
12. Edmonds, D. A., Toby, S. C., Siverd, C. G., Twilley, R., Bentley, S. J., Hagen, S., & Xu, K. (2023). Land loss due to human-altered sediment budget in the Mississippi River Delta. *Nature Sustainability*, 1–8. https://doi.org/10.1038/s41893-023-01081-0
13. Feng, Y., Sun, T., Zhu, M. S., Qi, M., Yang, W., & Shao, D. D. (2018). Salt marsh vegetation distribution patterns along groundwater table and salinity gradients in yellow river estuary under the influence of land reclamation. *Ecological Indicators*, *92*, 82–90. https://doi.org/10.1016/j.ecolind.2017.09.027
14. Goldberg, L., Lagomasino, D., Thomas, N., & Fatoyinbo, T. (2020). Global declines in human-driven mangrove loss. *Global Change Biology*, *26*(10), 5844–5855. https://doi.org/10.1111/gcb.15275
15. Huang, X., Duan, Y., Tao, Y., Wang, X., Long, H., Luo, C., & Lai, Y. (2022). Effects of Spartina alterniflora Invasion on Soil Organic Carbon Storage in the Beihai Coastal Wetlands of China. *Frontiers in Marine Science*, *9*. https://www.frontiersin.org/articles/10.3389/fmars.2022.890811
16. Li, G., Fang, C., & Qi, W. (2021). Different effects of human settlements changes on landscape fragmentation in China: Evidence from grid cell. *Ecological Indicators*, *129*, 107927. https://doi.org/10.1016/j.ecolind.2021.107927
17. Li, H., & Wu, J. (2004). Use and misuse of landscape indices. *Landscape Ecology*, *19*(4), 389–399. https://doi.org/10.1023/B:LAND.0000030441.15628.d6
18. Li, L., Li, X., Niu, B., & Zhang, Z. (2023). A Study on the Dynamics of Landscape Patterns in the Yellow River Delta Region. *Water*, *15*(4), Article 4. https://doi.org/10.3390/w15040819
19. Li, S., Xie, T., Bai, J., & Cui, B. (2022). Degradation and Ecological Restoration of Estuarine Wetlands in China. *Wetlands*, *42*(7), 90. https://doi.org/10.1007/s13157-022-01589-9
20. Li, Y., Dang, B., Zhang, Y., & Du, Z. (2022). Water body classification from high-resolution optical remote sensing imagery: Achievements and perspectives. *ISPRS Journal of Photogrammetry and Remote Sensing*, *187*, 306–327. https://doi.org/10.1016/j.isprsjprs.2022.03.013
21. Lin, Q., & Yu, S. (2018). Losses of natural coastal wetlands by land conversion and ecological degradation in the urbanizing Chinese coast. *Scientific Reports*, *8*(1), Article 1. https://doi.org/10.1038/s41598-018-33406-x
22. Liu, Y., Han, J., Jiao, J., Liu, B., Ge, W., Pan, Q., & Wang, F. (2022). Responses of flood peaks to land use and landscape patterns under extreme rainstorms in small catchments—A case study of the rainstorm of Typhoon Lekima in Shandong, China. *International Soil and Water Conservation Research*, *10*(2), 228–239. https://doi.org/10.1016/j.iswcr.2021.07.005

23. Loucks, D. P. (2019). Developed river deltas: Are they sustainable? *Environmental Research Letters*, *14*(11), 113004. https://doi.org/10.1088/1748-9326/ab4165
24. Ma, X., Yan, J., Wang, F., Qiu, D., Jiang, X., Liu, Z., Sui, H., Bai, J., & Cui, B. (2019). Trait and density responses of Spartina alterniflora to inundation in the Yellow River Delta, China. *Marine Pollution Bulletin*, *146*, 857–864. https://doi.org/10.1016/j.marpolbul.2019.07.022
25. Murray, N. J., Phinn, S. R., DeWitt, M., Ferrari, R., Johnston, R., Lyons, M. B., Clinton, N., Thau, D., & Fuller, R. A. (2019). The global distribution and trajectory of tidal flats. *Nature*, *565*(7738), Article 7738. https://doi.org/10.1038/s41586-018-0805-8
26. Murray, N. J., Worthington, T. A., Bunting, P., Duce, S., Hagger, V., Lovelock, C. E., Lucas, R., Saunders, M. I., Sheaves, M., Spalding, M., Waltham, N. J., & Lyons, M. B. (2022). High-resolution mapping of losses and gains of Earth's tidal wetlands. *Science*, *376*(6594), 744–749. https://doi.org/10.1126/science.abm9583
27. Nienhuis, J. H., Ashton, A. D., Edmonds, D. A., Hoitink, A. J. F., Kettner, A. J., Rowland, J. C., & Törnqvist, T. E. (2020). Global-scale human impact on delta morphology has led to net land area gain. *Nature*, *577*(7791), Article 7791. https://doi.org/10.1038/s41586-019-1905-9
28. Osland, M. J., Chivoiu, B., Enwright, N. M., Thorne, K. M., Guntenspergen, G. R., Grace, J. B., Dale, L. L., Brooks, W., Herold, N., Day, J. W., Sklar, F. H., & Swarzenzki, C. M. (2022). Migration and transformation of coastal wetlands in response to rising seas. *Science Advances*, *8*(26), eabo5174. https://doi.org/10.1126/sciadv.abo5174
29. Pang, B., Xie, T., Cui, B., Wang, Q., Ning, Z., Liu, Z., Chen, C., Lu, Y., & Zhao, X. (2023). Adaptability of Common Coastal Wetland Plant Populations to Future Sea Level Rise. *Ecosystem Health and Sustainability*, *9*, 0005. https://doi.org/10.34133/ehs.0005
30. Paszkowski, A., Goodbred, S., Borgomeo, E., Khan, M. S. A., & Hall, J. W. (2021). Geomorphic change in the Ganges–Brahmaputra–Meghna delta. *Nature Reviews Earth & Environment*, *2*(11), Article 11. https://doi.org/10.1038/s43017-021-00213-4
31. Reader, M. O., Eppinga, M. B., de Boer, H. J., Damm, A., Petchey, O. L., & Santos, M. J. (2022). The relationship between ecosystem services and human modification displays decoupling across global delta systems. *Communications Earth & Environment*, *3*(1), Article 1. https://doi.org/10.1038/s43247-022-00431-8
32. Reid, W. V. (2005). *Millennium Ecosystem Assessment: Ecosystems and Human Well-being*. https://www.wri.org/research/millennium-ecosystem-assessment-ecosystems-and-human-well-being
33. Rodríguez, J. F., Saco, P. M., Sandi, S., Saintilan, N., & Riccardi, G. (2017). Potential increase in coastal wetland vulnerability to sea-level rise suggested by considering hydrodynamic attenuation effects. *Nature Communications*, *8*(1), Article 1. https://doi.org/10.1038/ncomms16094
34. Rodriguez-Galiano, V. F., Ghimire, B., Rogan, J., Chica-Olmo, M., & Rigol-Sanchez, J. P. (2012). An assessment of the effectiveness of a random forest classifier for land-cover classification. *ISPRS Journal of Photogrammetry and Remote Sensing*, *67*, 93–104. https://doi.org/10.1016/j.isprsjprs.2011.11.002
35. Rosentreter, J. A., Laruelle, G. G., Bange, H. W., Bianchi, T. S., Busecke, J. J. M., Cai, W.-J., Eyre, B. D., Forbrich, I., Kwon, E. Y., Maavara, T., Moosdorf, N., Najjar, R. G., Sarma, V. V. S. S., Van Dam, B., & Regnier, P. (2023). Coastal vegetation and estuaries are collectively a greenhouse gas sink. *Nature Climate Change*, *13*(6), Article 6. https://doi.org/10.1038/s41558-023-01682-9
36. Shammi, S. A., & Meng, Q. (2021). Use time series NDVI and EVI to develop dynamic crop growth metrics for yield modeling. *Ecological Indicators*, *121*, 107124. https://doi.org/10.1016/j.ecolind.2020.107124
37. Song, S., Wang, S., Fu, B., Liu, Y., Wang, K., Li, Y., & Wang, Y. (2020). Sediment Transport under Increasing Anthropogenic Stress: Regime Shifts within the Yellow River, China. *Ambio*, *49*(12), 2015–2025. https://doi.org/10.1007/s13280-020-01350-8
38. Spencer, T., Schuerch, M., Nicholls, R. J., Hinkel, J., Lincke, D., Vafeidis, A. T., Reef, R., McFadden, L., & Brown, S. (2016). Global coastal wetland change under sea-level rise and related stresses: The DIVA Wetland Change Model. *Global and*

Planetary Change, *139*, 15–30. https://doi.org/10.1016/j.gloplacha.2015.12.018

39. Stumpf, A., & Kerle, N. (2011). Object-oriented mapping of landslides using Random Forests. *Remote Sensing of Environment*, *115*(10), 2564–2577. https://doi.org/10.1016/j.rse.2011.05.013
40. Sun, C., Li, J., Liu, Y., Zhao, S., Zheng, J., & Zhang, S. (2023). Tracking annual changes in the distribution and composition of saltmarsh vegetation on the Jiangsu coast of China using Landsat time series–based phenological parameters. *Remote Sensing of Environment*, *284*, 113370. https://doi.org/10.1016/j.rse.2022.113370
41. Tischendorf, L. (2001). Can landscape indices predict ecological processes consistently? *Landscape Ecology*, *16*(3), 235–254. https://doi.org/10.1023/A:1011112719782
42. Törnqvist, T. E. (2023). A river delta in transition. *Nature Sustainability*, 1–2. https://doi.org/10.1038/s41893-023-01104-w
43. Wan, S., Qin, P., Liu, J., & Zhou, H. (2009). The positive and negative effects of exotic Spartina alterniflora in China. *Ecological Engineering*, *35*(4), 444–452. https://doi.org/10.1016/j.ecoleng.2008.05.020
44. Wang, H., Yang, Z., Saito, Y., Liu, J. P., Sun, X., & Wang, Y. (2007). Stepwise decreases of the Huanghe (Yellow River) sediment load (1950–2005): Impacts of climate change and human activities. *Global and Planetary Change*, *57*(3), 331–354. https://doi.org/10.1016/j.gloplacha.2007.01.003
45. Wang, S., Fu, B., Piao, S., Lü, Y., Ciais, P., Feng, X., & Wang, Y. (2016). Reduced sediment transport in the Yellow River due to anthropogenic changes. *Nature Geoscience*, *9*(1), 38–41. https://doi.org/10.1038/ngeo2602
46. Wang, X., Xiao, X., Xu, X., Zou, Z., Chen, B., Qin, Y., Zhang, X., Dong, J., Liu, D., Pan, L., & Li, B. (2021a). Rebound in China's coastal wetlands following conservation and restoration. *Nature Sustainability*, *4*(12), Article 12. https://doi.org/10.1038/s41893-021-00793-5
47. Wang, X., Xiao, X., Xu, X., Zou, Z., Chen, B., Qin, Y., Zhang, X., Dong, J., Liu, D., Pan, L., & Li, B. (2021b). Rebound in China's coastal wetlands following conservation and restoration. *Nature Sustainability*, *4*(12), 1076–1083. https://doi.org/10.1038/s41893-021-00793-5
48. Ward, N. D., Megonigal, J. P., Bond-Lamberty, B., Bailey, V. L., Butman, D., Canuel, E. A., Diefenderfer, H., Ganju, N. K., Goñi, M. A., Graham, E. B., Hopkinson, C. S., Khangaonkar, T., Langley, J. A., McDowell, N. G., Myers-Pigg, A. N., Neumann, R. B., Osburn, C. L., Price, R. M., Rowland, J., … Windham-Myers, L. (2020). Representing the function and sensitivity of coastal interfaces in Earth system models. *Nature Communications*, *11*(1), Article 1. https://doi.org/10.1038/s41467-020-16236-2
49. Watts, J. D., Lawrence, R. L., Miller, P. R., & Montagne, C. (2009). Monitoring of cropland practices for carbon sequestration purposes in north central Montana by Landsat remote sensing. *Remote Sensing of Environment*, *113*(9), 1843–1852. https://doi.org/10.1016/j.rse.2009.04.015
50. Xia, H., Liu, L., Bai, J., Kong, W., Lin, K., & Guo, F. (2020). Wetland Ecosystem Service Dynamics in the Yellow River Estuary under Natural and Anthropogenic Stress in the Past 35 Years. *Wetlands*, *40*(6), 2741–2754. https://doi.org/10.1007/s13157-020-01368-4
51. Xia, X., Dong, J., Wang, M., Xie, H., Xia, N., Li, H., Zhang, X., Mou, X., Wen, J., & Bao, Y. (2016). Effect of water-sediment regulation of the Xiaolangdi reservoir on the concentrations, characteristics, and fluxes of suspended sediment and organic carbon in the Yellow River. *Science of The Total Environment*, *571*, 487–497. https://doi.org/10.1016/j.scitotenv.2016.07.015
52. Yu, D., Han, G., Wang, X., Zhang, B., Eller, F., Zhang, J., & Zhao, M. (2021). The impact of runoff flux and reclamation on the spatiotemporal evolution of the Yellow River estuarine wetlands. *Ocean & Coastal Management*, *212*, 105804. https://doi.org/10.1016/j.ocecoaman.2021.105804
53. Zeng, Y., Hao, D., Huete, A., Dechant, B., Berry, J., Chen, J. M., Joiner, J., Frankenberg, C., Bond-Lamberty, B., Ryu, Y., Xiao, J., Asrar, G. R., & Chen, M. (2022). Optical vegetation indices for monitoring terrestrial ecosystems globally. *Nature Reviews Earth & Environment*, *3*(7), Article 7. https://doi.org/10.1038/s43017-022-00298-5

54. Zhan, C., Wang, Q., Cheng, S., Zeng, L., Yu, J., Dong, C., & Yu, X. (2023). Investigating the evolution of landscape patterns in historical subdeltas and coastal wetlands in the Yellow River Delta over the last 30 years: A geo-informatics approach. *Frontiers in Marine Science*, *10*. https://www.frontiersin.org/articles/10.3389/fmars.2023.1115720
55. Zhang, C., Gong, Z., Qiu, H., Zhang, Y., & Zhou, D. (2021). Mapping typical salt-marsh species in the Yellow River Delta wetland supported by temporal-spatial-spectral multidimensional features. *Science of The Total Environment*, *783*, 147061. https://doi.org/10.1016/j.scitotenv.2021.147061
56. Zhang, X., Wang, G., Xue, B., Zhang, M., & Tan, Z. (2021). Dynamic landscapes and the driving forces in the Yellow River Delta wetland region in the past four decades. *Science of The Total Environment*, *787*, 147644. https://doi.org/10.1016/j.scitotenv.2021.147644
57. Zhang, Y., Wang, X., Yan, S., Zhu, J., Liu, D., Liao, Z., Li, C., & Liu, Q. (2022). Influences of Phragmites australis density and groundwater level on soil water in semiarid wetland, North China: Which is more influential? *Ecohydrology & Hydrobiology*, *22*(1), 85–95. https://doi.org/10.1016/j.ecohyd.2021.07.001
58. Zhou, K. (2022). Wetland landscape pattern evolution and prediction in the Yellow River Delta. *Applied Water Science*, *12*(8), 190. https://doi.org/10.1007/s13201-022-01711-6
59. Google Earth Engine (2023a). USGS Landsat 8 Level 2, Collection 2, Tier 1 | Earth Engine Data Catalog. https://developers.google.com/earth-engine/datasets/catalog/LANDSAT_LC08_C02_T1_L2/ (accessed 13 April 2023).
60. Google Earth Engine (2023b). Sentinel-2 MSI: MultiSpectral Instrument, Level-2A | Earth Engine Data Catalog. https://developers.google.com/earth-engine/datasets/catalog/COPERNICUS_S2_SR/ (accessed 13 April 2023).

Figures

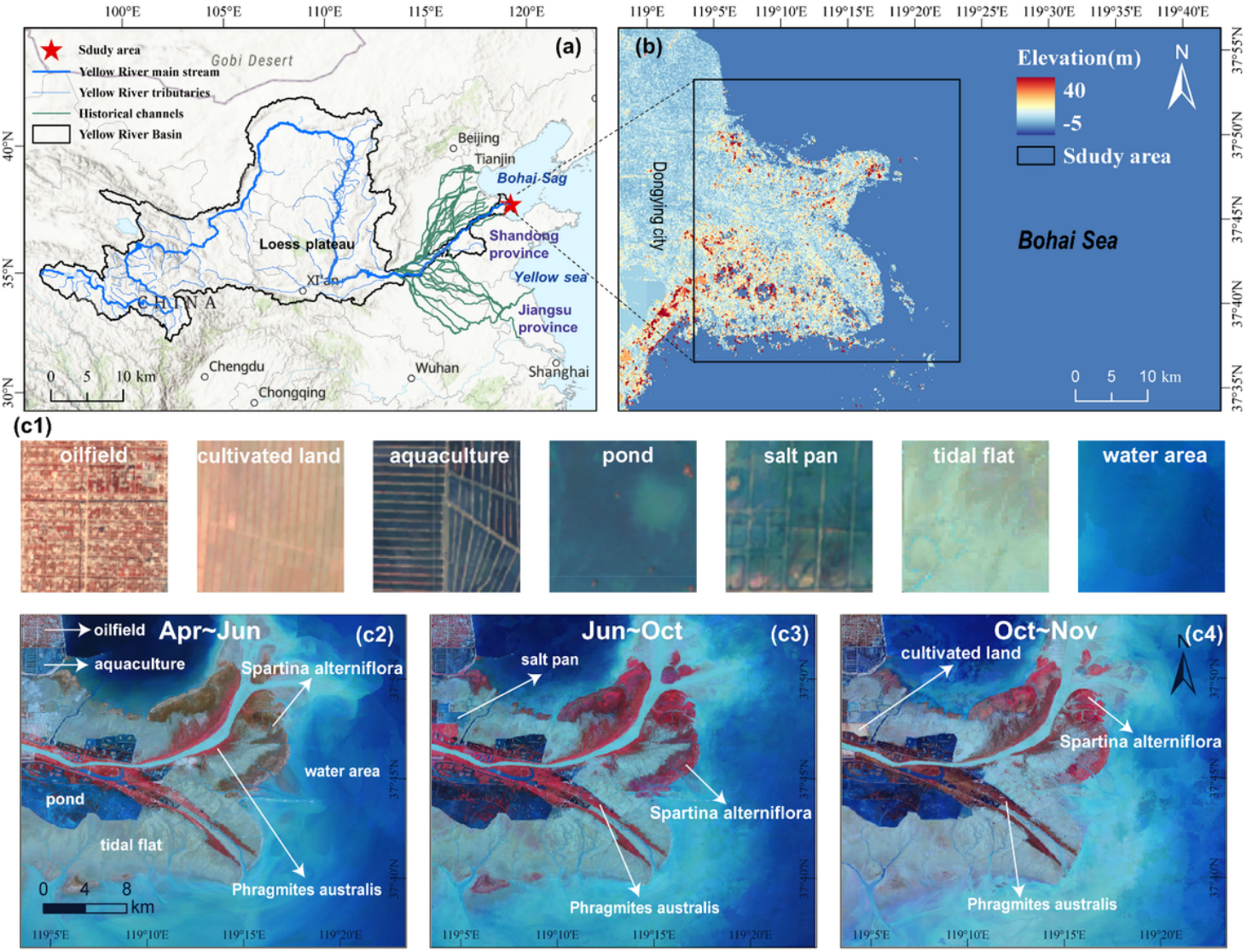


Figure 1

Location (a), elevation (b) of the YRD (Yellow River Delta) wetland and interpretive markers of wetland patches in the YRD wetland (c1-c4)

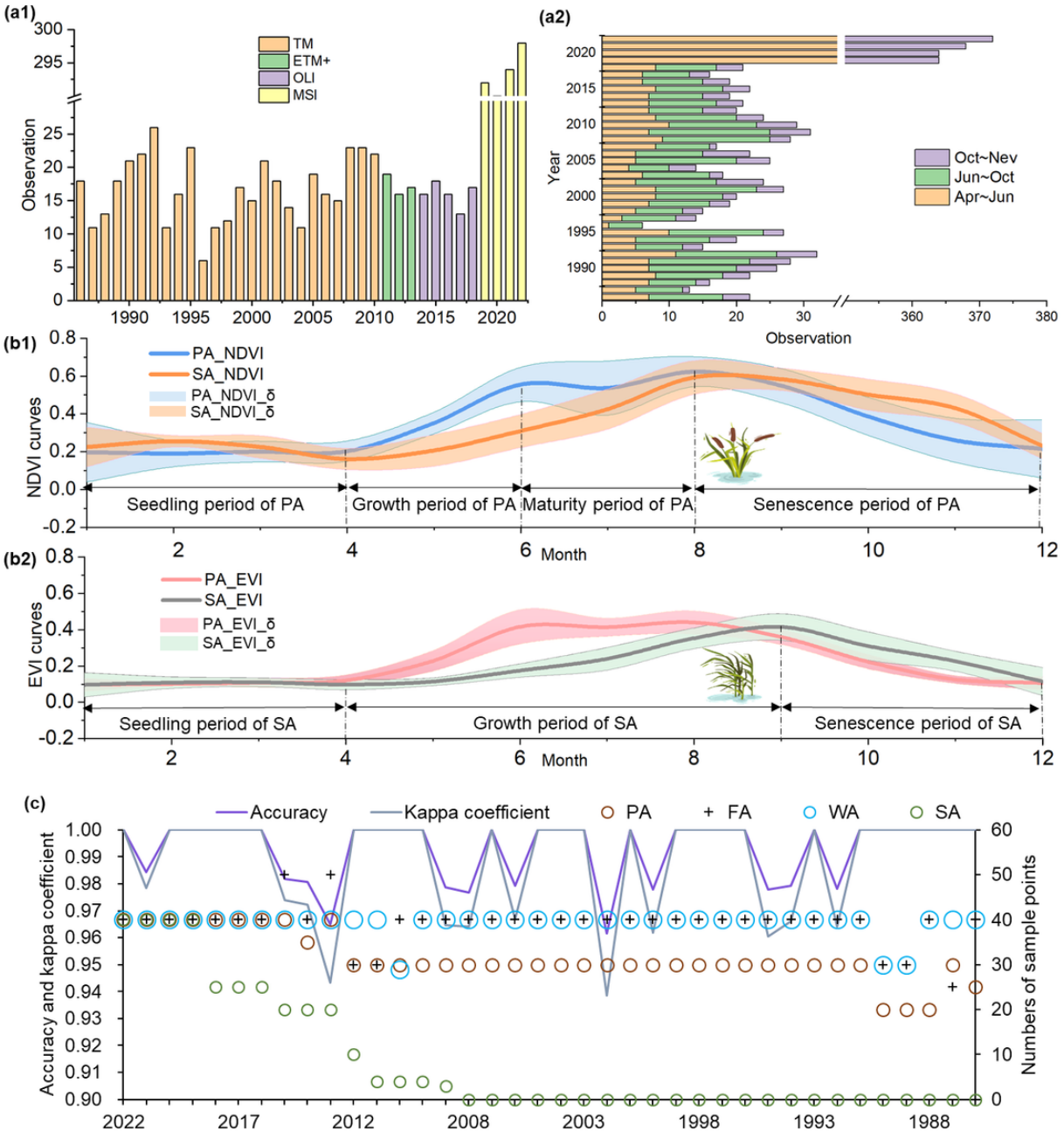


Figure 2

Available Landsat and Sentinel observation numbers for different sensors and periods during 1986–2022 (a1-a2), NDVI/EVI curves and standard deviation of PA and SA (b1-b2), number of different samples, accuracy and Kappa coefficient of supervised classification (c). (b1-b2) The solid line is the mean value of NDVI/EVI during 2011-2021, and the semi-transparent band represents the total standard deviation (δ). The dotted line divides the life cycle of the PA/SA. PA, SA, FA, WA and represent *Phragmites australis, Spartina alterniflora*, tidal flat and water body respectively

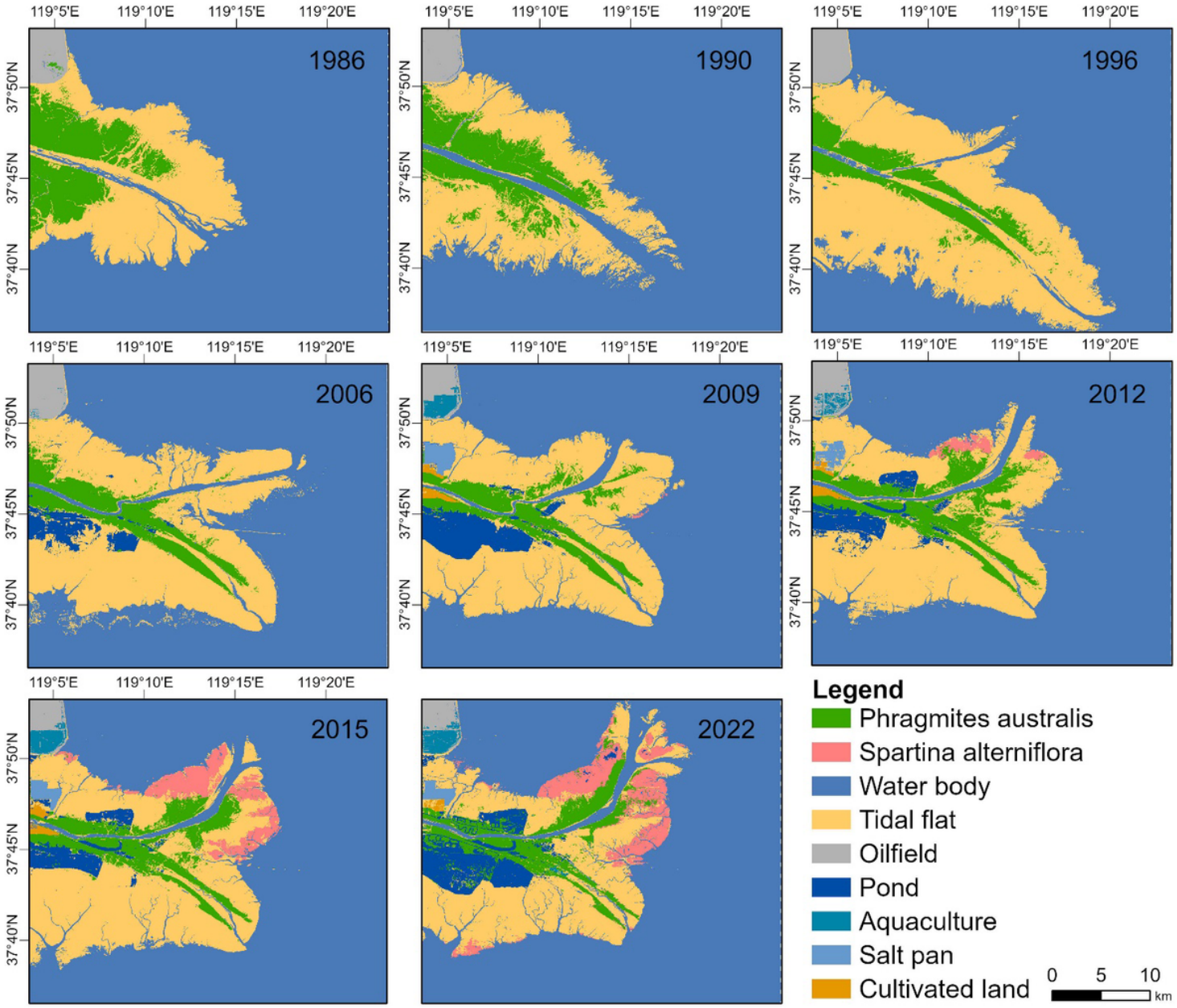


Figure 3

Eight representative spatial maps of typical saltmarshes in the YRD wetland were selected from 1986 to 2022

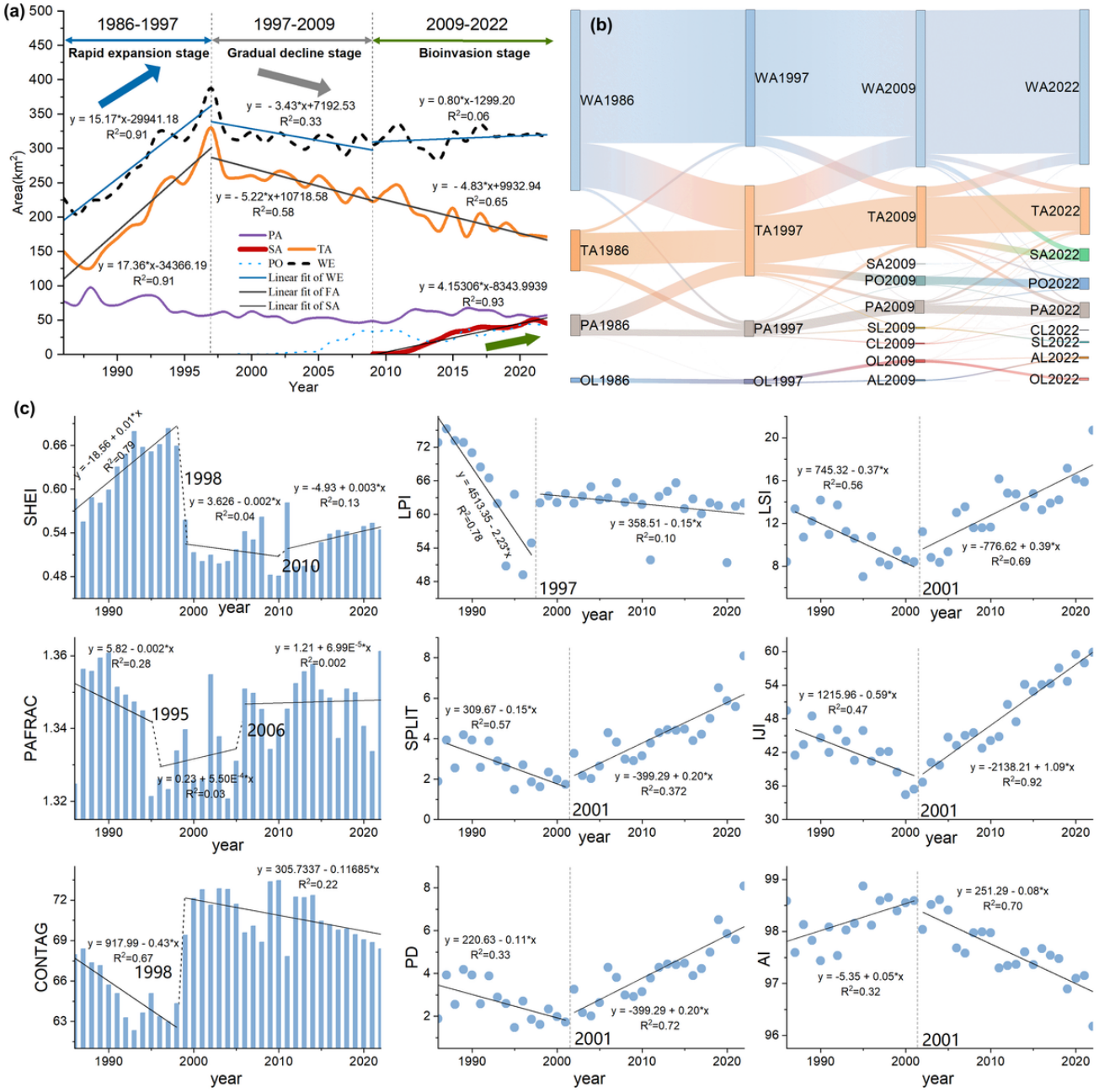


Figure 4

Three phases of the wetland landscape evolution in the YRD wetland during 1986-2022. (a) Temporal variation curve and piecewise linear fitting line of wetland typical patch area from 1986 to 2022. (b) Sankey map of wetland patch transfer at four key time nodes (1986,1997,2009,2022). (c) Inter-annual variation and piecewise linear trend fitting of wetland landscape indices in the YRD wetland from 1986 to 2022. PA, SA, TA, PO, and WE represent the areas of *Phragmites australis*, *Spartina alterniflora*, tidal flat, pond, and wetland, respectively. The wetland area is the sum of the SA, PA, PO, and TA areas. WA, SL, CL, OL and AL represent the areas of water bodies, salt pans, cultivated land, oilfield, and aquaculture, respectively

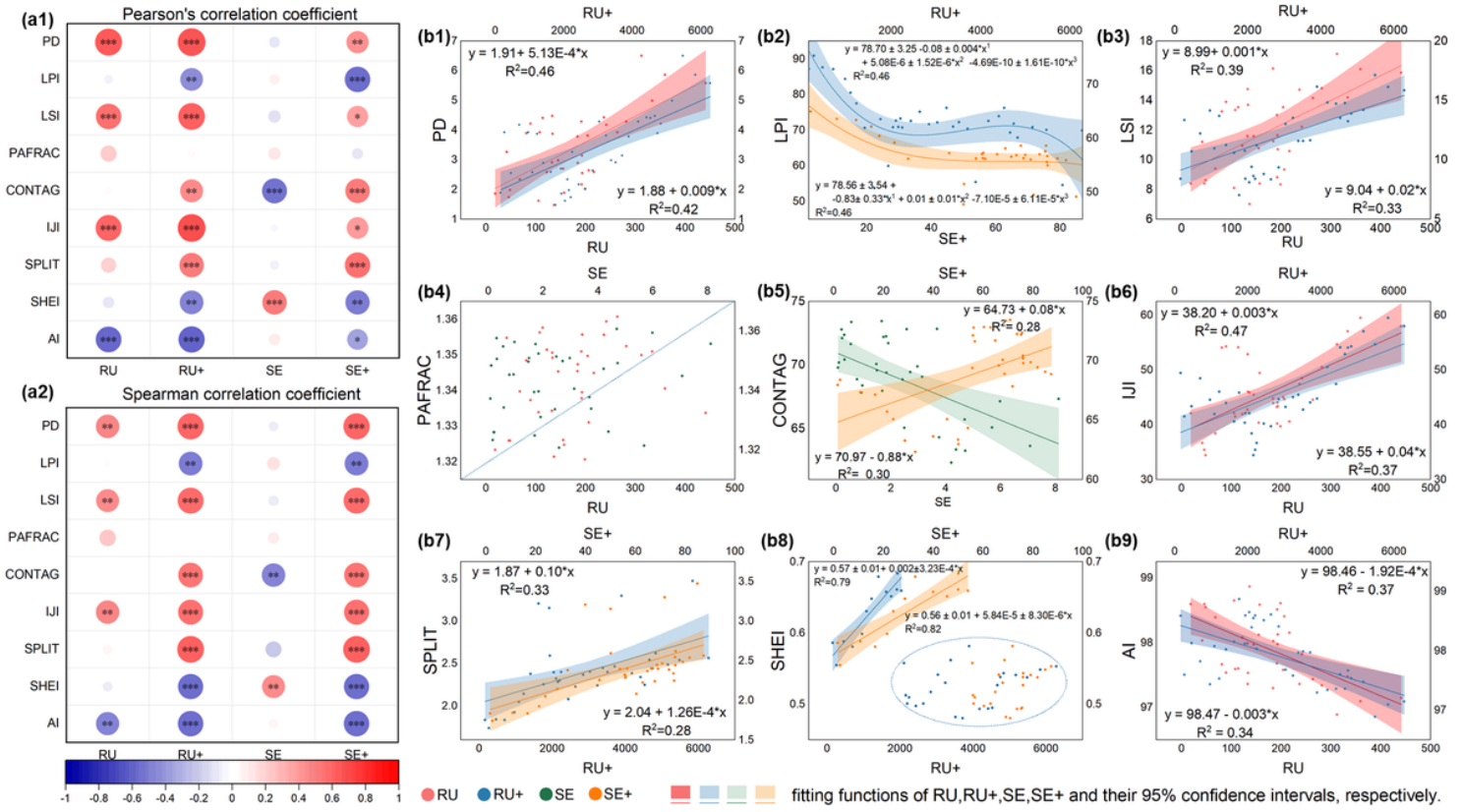


Figure 5

Pearson and Spearman correlation coefficient matrix of landscape indices with hydrological drivers (a1-a2), and function fitting and scatter plots between them (b1-b9). Where, RU, RU+, SE, and SE+ respectively represent the runoff, cumulative runoff, sediment discharge and cumulative sediment discharge of the Lijin hydrographic station. The fitting function and R^2 of the landscape index with a specific hydrological variable are displayed at the intersection of the two axes (except for SHEI, where the display of the fitting function and R^2 follows the nearest principle)

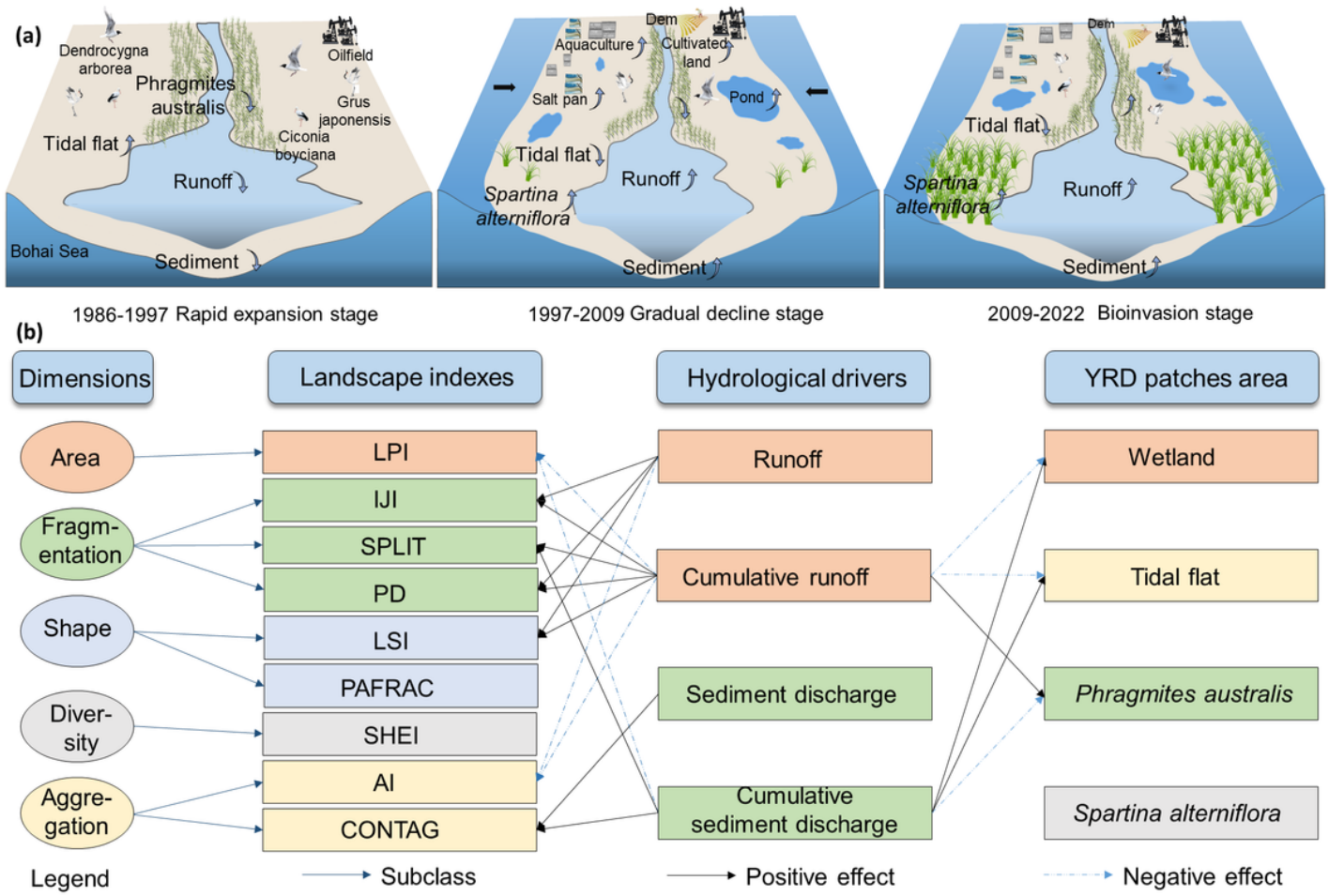


Figure 6

Landscape pattern evolution diagrammatic drawing of YRD wetland (a), and hydrological driving factors of wetland landscape pattern evolution (b). The arrows in the diagrammatic drawing represent the trend of the typical patch area during this period